LETTER • OPEN ACCESS

Heat metrics and thresholds reshape population exposure and inequality signals

To cite this article: Liutao Chen *et al* 2026 *Environ. Res. Lett.* **21** 094022

ENVIRONMENTAL RESEARCH
LETTERS

OPEN ACCESS

RECEIVED
10 March 2026

REVISED
20 April 2026

ACCEPTED FOR PUBLICATION
30 April 2026

PUBLISHED
12 May 2026

LETTER

Heat metrics and thresholds reshape population exposure and inequality signals

Liutao Chen[1], **TC Chakraborty**[2], **Joan A Casey**[3,4], **Ching-Hsuan Huang**[3] and **Tzu-Hsin Karen Chen**[1,3,*]

[1] Department of Urban Design and Planning, University of Washington, Seattle 98105 WA, United States of America
[2] Pacific Northwest National Laboratory, Richland 99352 WA, United States of America
[3] Department of Environmental and Occupational Health Sciences, University of Washington, Seattle 98105 WA, United States of America
[4] Department of Epidemiology, University of Washington, Seattle 98105 WA, United States of America
[*] Author to whom any correspondence should be addressed.

E-mail: kthchen@uw.edu

Keywords: extreme heat, heat exposure, hotspot agreement, environmental justice, socioeconomic deprivation, Mediterranean

Supplementary material for this article is available online

Abstract

Extreme heat is intensifying worldwide, yet estimates of heat hazard and exposure inequality depend on both the heat metric and how extreme days are defined. Using summer 2022 across the Mediterranean, we quantify population heat exposure with four metrics—land surface temperature (LST), air temperature (Ta), heat index (HI), and wet-bulb globe temperature (WBGT)—under absolute (fixed-value) and relative (anomaly-based) thresholds. Under absolute thresholds, total heat exposure differs by more than two orders of magnitude across metrics (31.3 billion person-days for Ta vs 0.3 billion for HI). Geographic hotspots also diverge: WBGT concentrates in humid coastal North Africa (e.g. the Nile Delta), whereas Ta and LST are more widespread. Under relative thresholds, exposure totals converge and cross-metric hotspot agreement increases (e.g. Ta–WBGT top-tercile overlap increases from 10.7% to 29.0%), shifting hotspots toward densely populated southern Europe. Crucially, the exposure–deprivation relationship also reverses across threshold frameworks: absolute thresholds concentrate exposure in more deprived North Africa and the Middle East, whereas relative thresholds shift the burden toward less-deprived European cities. This sensitivity is decision-relevant: city rankings based on WBGT exposure duration are almost completely reordered when switching threshold frameworks. Threshold choice therefore systematically reshapes hotspot patterns and inequality signals. Reporting both absolute and relative exposures can reveal hidden hotspots and support more targeted heat-risk monitoring and intervention planning.

1. Introduction

Extreme heat exposure is intensifying under climate change and increasingly threatens human health, labor productivity, and economic output [1–5]. Heat exposure is also socially patterned: disadvantaged populations often face higher hazards and have fewer protective resources, so assessing exposure is essential for understanding and addressing heat-exposure inequalities [4, 6, 7]. By integrating climate and demographic data, exposure assessments can support targeted interventions, early warning systems, and scenario planning [8–10]. Yet estimated exposure and inferred inequalities depend strongly on metric and threshold choices, potentially altering which places and populations are prioritized for intervention [11].

Heat metric choice reflects health relevance, operational use, and data availability. Thermal infrared satellite observations provide spatially explicit land surface temperature (LST) for mapping surface heat patterns across scales [12–14]. Available at kilometer or finer resolution, LST is often an overpass-time snapshot that reveals thermal heterogeneity missed by coarser atmospheric products. However, LST is not equivalent to near-surface air conditions experienced by people [15]. Air temperature (Ta) aligns with

weather forecasting and public communication and is often available hourly, but it does not account for humidity, which constrains evaporative cooling [16]. Temperature-only metrics can therefore underestimate heat stress in humid settings [17, 18]. Composite indices, such as heat index (HI) and wet-bulb globe temperature (WBGT), integrate multiple drivers and better reflect physiological heat load, but they weigh humidity, radiation, and wind differently, which can change hazard assessments [19–22].

A second key choice in heat exposure assessment is how to define extremes. Absolute thresholds use fixed values intended to capture conditions approaching physiological limits [17] and are widely used to trigger actions such as heat alerts or occupational protections [21, 23, 24]. However, universal thresholds are difficult to justify because acclimatization and adaptation vary across populations [25, 26]. Relative thresholds instead identify extremes against local climatology and are widely used in climate-extremes research and warning systems [1, 27]. Yet the 90th or 95th percentiles may not always reach thermally stressful levels, while harmful conditions may occur at lower percentiles [28]. Because absolute and relative thresholds capture different risk dimensions—fixed-condition burden versus local anomaly—threshold choice can reshape exposure totals, hotspot geography, and affected populations [1].

These metric and threshold choices may result in substantial differences in exposure magnitude and hotspot locations (table S1), especially in regions spanning diverse climates. Temperature-based metrics tend to yield more frequent extremes in dry–hot environments [29, 30], while moisture- and radiation-informed indices better capture dangerous humid-heat conditions in coastal climates [4, 19, 29, 31]. In such settings, these choices can reshape hotspot geography and the distribution of exposed populations.

The Mediterranean provides a useful testbed for broader heat-exposure research because humid coastlines and arid interiors coexist across a dense network of cities and settlements with diverse socioeconomic conditions. It is also a climate-change hotspot, with warming and heat extremes intensifying across the basin, particularly in the southern and eastern Mediterranean [1, 5, 32–34]. Populations are concentrated along the southern and eastern coasts, increasing the potential for uneven exposure [33, 35, 36]. The heatwaves of 2022 led to 61 672 heat-related deaths in Mediterranean-adjacent European countries, underscoring the need to understand how heat burden is characterized across this heterogeneous region [37].

Despite growing work on heat exposure, evidence remains limited on how heat metrics and threshold frameworks jointly shape estimated exposure, hotspot geography, and inequality patterns [38, 39], partly because most studies examine a narrow set of indicators or only a few cities (table S1). The implications of methodological choices therefore remain unclear at the regional scale [6, 7].

Here, we quantify population heat exposure across Mediterranean countries during summer 2022 using four widely used metrics (LST, Ta, HI, and WBGT) under absolute and relative thresholds. We compare exposure duration (person-days), exceedance-based intensity (person-day-degrees; hereafter, intensity), cross-metric hotspot agreement, and variation in exposure by deprivation. Specifically, we ask: (1) how duration and intensity differ across metrics and threshold frameworks; (2) how consistently different metrics identify hotspots under each threshold; and (3) how exposure–deprivation associations change across metric–threshold combinations. These comparisons show how metric and threshold choices reshape inferred exposure patterns and spatial priorities for heat-action planning. A schematic overview of the study design and comparison framework is provided in figure S1.

2. Materials and methods

2.1. Data sources

The analysis spans the summer period from 15 June to 15 September 2022 across the Mediterranean region. All datasets are resampled to a common 1 km analysis grid (table 1). Population for 2022 is derived from the global human settlement layer (GHSL) by pixel-wise linear interpolation between 2020 and 2025; GHSL urban boundaries (2020) are used to define urban settlement areas for city-level aggregation. Daytime LST is obtained from the MODIS Aqua MYD11A1 product, with pixel-level quality control applied to retain only data with an uncertainty of $\leqslant 3$ °C and thereby reduce cloud-related errors [40]. Meteorological variables are sourced from ERA5-Land, including 2 m Ta, dew point temperature (Td), downward shortwave radiation (K↓), and 10 m wind speed (WS) (figure S2). Socioeconomic conditions are characterized using the global gridded relative deprivation index (GRDI; 30 arc-second, ∼1 km; 0–100, higher = more deprivation) [41], which is reprojected and aligned to the 1 km analysis grid. To examine deprivation-exposure patterns at the city level, we compute city-level total exposure and mean deprivation within GHSL urban boundaries [42]. Following the Organization for Economic Co-operation and Development classification, cities are grouped by population-size categories: small (<200 000), medium (200 000–500 000), metropolitan (500 000–1 500 000), and large metropolitan ($\geqslant$1.5 million).

2.2. Heat metrics

We quantify heat exposure using four metrics: daytime LST, daily maximum 2 m Ta, HI, and WBGT.

Table 1. Input datasets used in this study.

Data source	Variable(s)	Temporal Scope	Resolution
Global human settlement layer	Population count	2022 (interpolated)	1 km
Global human settlement layer	Urban boundary	2020	1 km
MODIS aqua (MYD11A1)	Land surface temperature (LST)	Jun 15–Sep 15, 2022	1 km
ERA5-Land reanalysis	2 m air temp (Ta), dewpoint temp (Td), downward shortwave radiation (K↓), Wind speed (WS)	Jun 15–Sep 15, 2022	∼ 11 km
NASA socioeconomic data and applications center	Global gridded relative deprivation index (GRDI)	2020	∼1 km

LST represents a radiative surface temperature proxy at the MODIS Aqua overpass time (∼13:30 local time) [12, 43], whereas Ta represents air temperature from ERA5-Land. For HI and WBGT, we compute hourly fields and extract local-time daily maxima to represent peak heat stress.

HI is computed following the NOAA algorithm [44] using hourly Ta and relative humidity (RH), with RH derived from Ta and Td using a standard vapor-pressure formulation. HI is then estimated using the NOAA Rothfusz regression with the low- and high-humidity adjustments [44] (*supplementary methods*). WBGT integrates temperature, humidity, radiation, and wind and is widely used in occupational heat-stress guidance [45]. Because direct calculation of natural wet-bulb temperature and black-globe temperature requires variables not available from ERA5-Land, we estimate WBGT using the proxy method of Carter *et al* [46], which uses Ta, RH, K↓, and WS and follows the Kestrel monitor implementation [46, 47] (*supplementary methods*). We use this approach because it is compatible with the available ERA5-Land inputs and has an observationally evaluated basis, although independent validation data for the Mediterranean remain needed.

2.3. Definitions of extreme heat and burden metrics

For each metric, we define extreme-heat days using two threshold frameworks: absolute thresholds, which apply fixed values motivated by commonly used health, safety, or operational guidance (table 2), and relative thresholds, which define extremes as daily values exceeding the local 90th percentile of the historical summer-day distribution over 2003–2022. We use the 90th percentile because it is widely adopted in climate-extremes and heat-exposure studies, supports comparison across locations with different climatological baselines, and avoids relying solely on rarer upper-tail exceedances [1, 12, 48].

We quantify population heat exposure at each 1 km grid cell i using two measures: (i) exposure duration and (ii) exceedance-based intensity (hereafter, intensity). The exposure duration D_i (person-days) is defined as:

$$D_i = \mathrm{Pop}_i \times \mathrm{Days}_i,$$

where Pop_i is the population count, and Days_i is the number of days on which the daily metric exceeds the applicable threshold (absolute or relative).

Intensity I_i for grid cell i (person-day-degrees) is defined as:

$$I_i = \mathrm{Pop}_i \times \sum_{d=1}^{n} \max\left(0, M_{i,d} - \mathrm{Thresh}_i\right),$$

where $M_{i,d}$ is the daily value of the metric on day d, and Thresh_i is the corresponding threshold. The summation runs over all days in the study period. For absolute thresholds, Thresh_i is spatially constant. For relative thresholds, Thresh_i varies by grid cell based on the 2003–2022 local percentile baseline. When $M_{i,d} \leqslant \mathrm{Thresh}_i$, the exceedance term equals zero and does not contribute.

2.4. Hotspot identification and agreement analysis

To assess hotspot agreement, we derive hotspot classes from exposure duration by classifying exposed pixels into low, medium, and high terciles using positive values pooled across the Mediterranean domain. Cross-metric agreement is evaluated using a bivariate tercile framework within pixels where both metrics were available, and at least one metric had a non-zero exposure duration. High-hotspot overlap is defined as the proportion of pixels classified as high by both metrics among those classified as high by either metric. For country-level summaries, the same Mediterranean-wide tercile thresholds are applied within each country; maps are aggregated to 10 km for display only, while statistics are computed at 1 km.

2.5. Heat exposure–deprivation analysis

To assess socioeconomic gradients in heat burden, we use the GRDI [41, 64]. GRDI is a 0–100 relative deprivation index (higher values indicate greater deprivation) built from six components: child dependency ratio, infant mortality rate, subnational human development index, built-up area ratio, nighttime-light intensity in 2020, and nighttime-light trend [64]. Because GRDI is designed to represent

Table 2. Definition of extreme heat day thresholds and metric interpretation. Note: relative thresholds for all metrics are defined using the local summer-season 90th percentile baseline (2003–2022).

Metric	Definition	Absolute threshold	Health implications for the absolute threshold	Application (who uses this metric)
LST	Land surface temperature	40 °C	Calibrated surface-temperature threshold approximating a hot-day air-temperature criterion (Ta ⩾ 30 °C; section 2.6)	Urban heat island studies [12, 49, 50]; policy monitoring [51, 52]; interpret with caution for exposure/health risk [15, 53]
Ta	Air temperature	30 °C	Temperature-only hot-day threshold representing conditions associated with elevated heat stress risk [2]	Climate monitoring/ assessment (IPCC) [33, 54]; public health epidemiology (most common; scalable data) [55–58]
HI	Heat index, human-perceived temperature based on Ta and RH	40.6 °C	A critical humid heat level associated with heat stroke, heat cramps, and heat exhaustion under shaded conditions [59]	U.S. National Weather Service (NWS) "Danger" category for public guidance [44, 60]; occupational heat guidance (OSHA) [21]
WBGT	Wet-bulb globe temperature, a composite index integrating Ta, RH, WS, K↓	30 °C	Outdoor heat load under conditions warranting protective actions for acclimatized individuals [23]	Occupational/military heat-stress guidance [23, 61]; validated for physiological strain [62]; NWS WBGT operational estimates [63]

relative deprivation and may not fully capture intra-urban differentials, we use it as a proxy for multidimensional deprivation in our analysis [64]. We resample GRDI to the 1 km analysis grid to align it with exposure estimates.

We characterize distributional inequality using deprivation-ranked burden curves. For each metric–threshold combination, exposed pixels are ranked by GRDI from least to most deprived, and we compute the cumulative share of population (x-axis) and cumulative share of total exposure burden (y-axis; using exposure duration, Di, and intensity, Ii). The 45° line denotes proportional burden; departures from this line indicate unequal exposure distribution across deprivation ranks.

Deprivation-stratified analyses are restricted to pixels with non-zero exposure duration ($D_i > 0$). Because GRDI has incomplete spatial coverage in some locations, we impute missing GRDI values only for deprivation-related analyses (not for total exposure estimates). Specifically, for exposed pixels with missing GRDI, we assign the nearest valid GRDI pixel within the same national boundary to avoid cross-border assignment; if the nearest valid pixel lies within 10 km, we use its GRDI value; otherwise, we assign the country-level median computed from valid pixels in that country. For the WBGT-based deprivation analysis, 25.3% of exposed pixels are assigned GRDI values via within-country nearest-neighbor matching, and 2.8% are assigned values via the country-level median.

2.6. Justification of the absolute LST threshold

LST and Ta represent different physical quantities—radiative surface temperature versus 2 m air temperature—and therefore generally do not share the same absolute hot-day threshold [65]. Figures 1(a) and (b) contrast the summer mean of daily maximum LST and Ta, highlighting their distinct spatial patterns and magnitude differences. To derive a physiologically interpretable absolute LST benchmark comparable to Ta ⩾ 30 °C, we calibrate the empirical relationship between daily maximum LST and Ta using up to 100 spatially distributed urban points per country selected via farthest-point sampling. The fitted linear model (figure 1(c), $\mathrm{LST} = 0.72 \times \mathrm{Ta} + 18.05$, $R^2 = 0.36$) indicates that Ta = 30 °C corresponds to LST ≈ 40 °C, whereas an uncalibrated LST ⩾ 30 °C would correspond to much milder Ta. Consistent with this calibration, LST ⩾ 40 °C better matches Ta ⩾ 30 °C in both exposure duration and intensity than does LST ⩾ 30 °C (figure 1(d)). We therefore adopt LST ⩾ 40 °C as the absolute threshold for subsequent LST-based analyses.

2.7. Software and computational environment

All heat-metric calculations and spatial analyses are conducted in Python 3.9, with cloud-based geospatial processing implemented through the Google Earth Engine (GEE [66]) Python API. Post-processing, statistical analyses, and figure generation are performed in Python using standard scientific, statistical, and geospatial libraries.

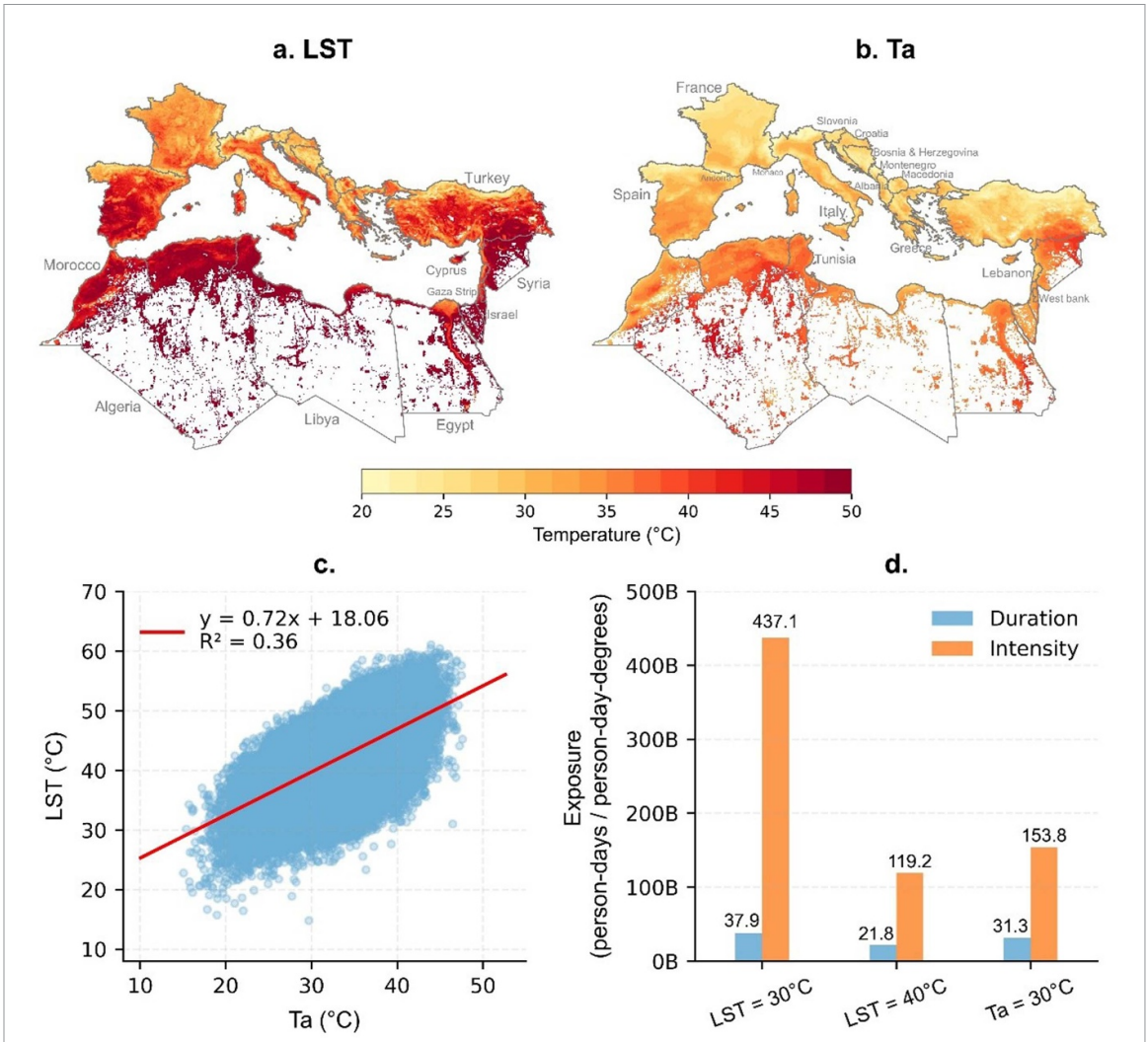

Figure 1. Spatial contrast between LST and Ta and calibration of an absolute LST threshold in summer 2022. (a) and (b) summer mean of daily maximum LST and Ta across the Mediterranean populated area (10 km aggregation for visualization). (c) Relationship between daily maximum LST and Ta across sampled urban points, with linear fit. (d) Comparison of exposure duration (person-days) and intensity (person-day-degrees) under candidate absolute thresholds; totals are reported in billions (B).

3. Results

3.1. Cross-metric contrasts in exposure duration and intensity

Under absolute thresholds, exposure duration differs markedly by metric (figure 2(a)). Ta yields 31.3 billion person-days, followed by LST (21.8 billion), WBGT (3.1 billion), and HI (0.3 billion), spanning more than two orders of magnitude between Ta and HI. Intensity follows the same ordering and further widens differences across metrics (figure 2(b)): totals are 153.8, 119.2, 2.1, and 0.3 billion person-day-degrees for Ta, LST, WBGT, and HI, respectively. Pixel-level distributions are strongly right-skewed for all metrics (figures 2(c) and (d)), indicating that regional totals are disproportionately driven by a limited number of hotspots. This concentration is especially pronounced for WBGT: median intensity is low (∼44 person-day-degrees), whereas the mean-to-median ratio is high (∼74).

Under relative thresholds, cross-metric differences in both duration and intensity largely diminish (figures 2(a) and (b)). Total exposure duration converges to 6.2–7.3 billion person-days and intensity remains tightly clustered across metrics. Because percentile-based thresholds classify extremes relative to local baselines, similar regional totals can arise even when hotspot locations differ. We next examine cross-metric agreement in hotspot locations.

3.2. Spatial agreement among heat metrics

Under absolute thresholds, hotspot patterns diverge across metrics (figure 3). Ta produces the broadest high-duration footprint spanning humid coasts and arid interiors, with prominent burdens in Egypt, Algeria, and Turkey. In contrast, WBGT concentrates high-duration exposure in humid coastal zones and the Nile Delta. LST broadly resembles Ta but with lower duration, whereas HI shows comparatively limited duration. Consistent with these differences,

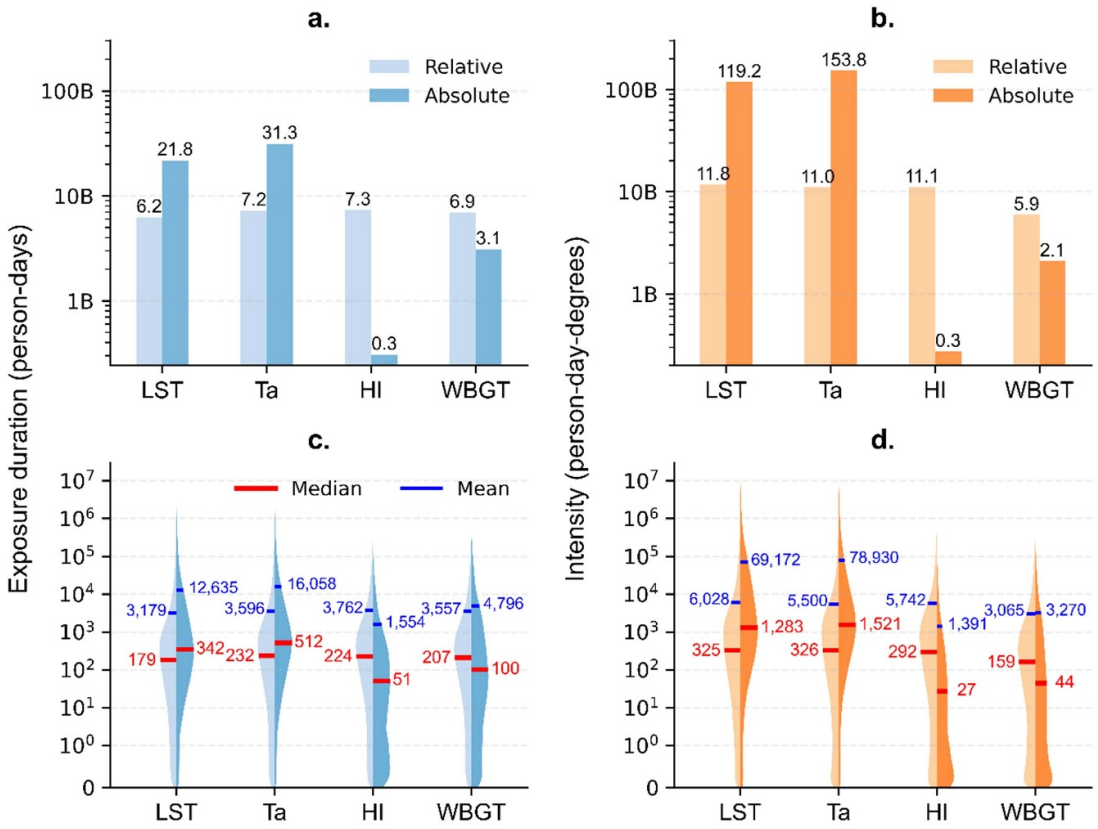

Figure 2. Heat exposure estimates across the Mediterranean under four metrics and two threshold frameworks. (a) Exposure duration (person-days) and (b) intensity (person-day-degrees) for LST, Ta, HI, and WBGT under relative and absolute thresholds; log *y*-axes; 'B' denotes values in billions. Pixel-level density distributions of (c) exposure duration and (d) intensity; for each metric, kernel density estimates are shown for the relative and absolute thresholds on the left and right sides, respectively, computed using pixels with positive values. Red and blue lines denote medians and means, respectively; colors match (a) and (b).

Ta–WBGT High–High pixels comprise 10.7% of evaluated pixels (figure 4(a); table S2); when focusing only on high hotspots (top-tercile union as denominator), overlap is 31.9% (figure 4(c)). Other metric pairs show similarly limited overlap under absolute thresholds (figures S3 and S4). Country summaries show that within-country overlap is highest in humid/coastal or geographically compact settings (e.g. Israel 77.9%), whereas arid interior regions more often fall into High Ta–Low WBGT classes (e.g. Turkey 20.8%). Top-decile co-hotspots are disproportionately located in North Africa across multiple pairs (table S3). Intensity patterns can also diverge across metrics (figure S8).

City-scale examples illustrate how these differences arise at finer scales (figures S9 and S10). Terciles are computed within each city to emphasize intra-urban contrasts in exposure duration. LST captures strong surface-property contrasts, whereas Ta is spatially smoother because it represents a coarser, background atmospheric field and contains limited explicit urban signal [67, 68], which can increase off-diagonal classes in heterogeneous urban–peri-urban mosaics. In Cairo (figure S9), irrigated/vegetated areas fall into Low LST–High Ta, consistent with surface cooling while Ta remains largely governed by the broader atmospheric background. In Bursa (figure S10), high Ta exposure duration extends over a broader surrounding area, whereas high LST exposure is concentrated in the dense built-up core. Paris exhibits mixed joint patterns consistent with heterogeneous land cover, whereas the more homogeneous desert setting of Ouargla yields joint patterns concentrated in High–High classes. Together, these cases indicate that hotspot agreement depends on both thresholding and the spatial representativeness of each heat product.

Under relative thresholds, spatial patterns become more consistent across metrics (figure 3), with high exposure duration expanding across populous southern Europe (e.g. France, Italy, Spain), and comparatively weaker signals over persistently hot parts of North Africa. Accordingly, Ta–WBGT High–High pixels increase to 29.0% (figure 4(b)), and high-hotspot overlap rises to 79.9% (figure 4(d)), with consistently higher overlap across pairs (74.7%–92.4%; figure 4(d), figures S5 and S6). This city-level pattern mirrors the regional results, with more diagonal joint patterns under relative thresholds (figures S11 and S12). Thus, moving from absolute to relative

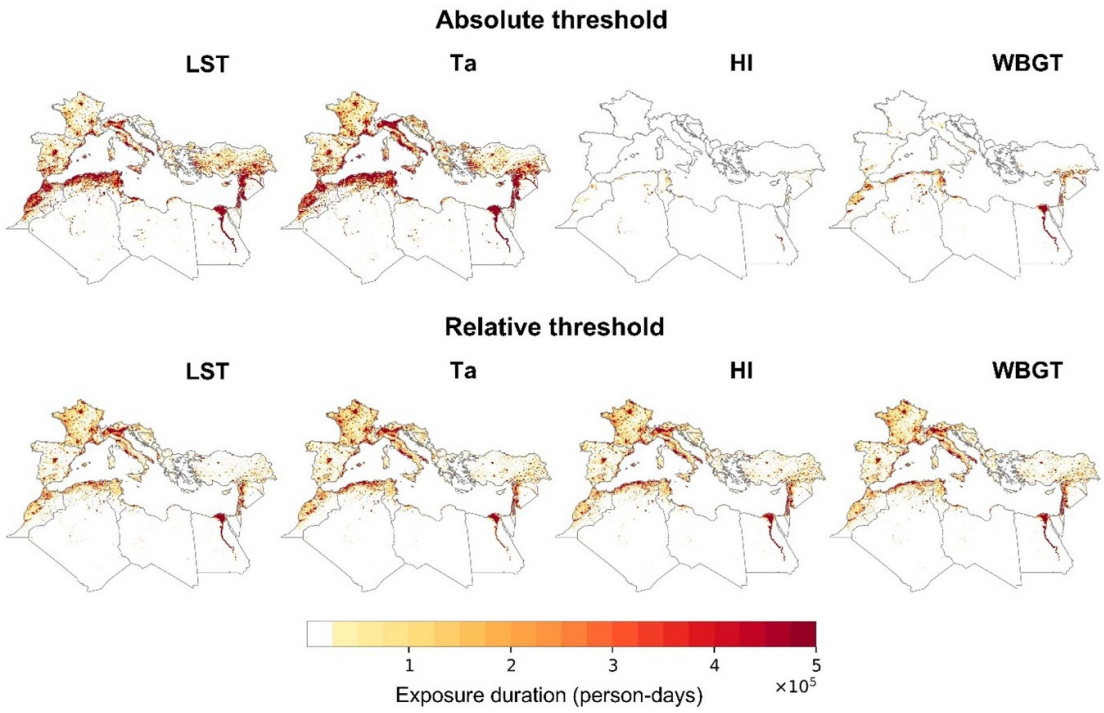

Figure 3. Spatial distribution of exposure duration across metrics and threshold frameworks. Exposure duration (person-days) for LST, Ta, HI and WBGT under absolute thresholds (top) and relative thresholds (bottom). For visual clarity, outputs are aggregated to 10 km for display.

thresholds increases cross-metric concordance and shifts the regional hotspot focus from North Africa toward densely populated southern Europe. Figure S7 visualizes this threshold-driven hotspot shift, showing that absolute thresholds often yield higher LST/Ta duration over North Africa, whereas relative thresholds more often yield higher HI/WBGT duration across southern Europe. These contrasts show that metric–threshold choices jointly determine which locations are identified as high-burden hotspots.

3.3. Socioeconomic inequality in heat-exposure burden

Deprivation-ranked burden curves show that switching between absolute and relative thresholds redistributes exposure along the GRDI gradient (figures 5(a) and S13). At the Mediterranean scale, a clear socioeconomic reversal emerges between threshold frameworks. Under absolute thresholds, exposure duration shifts toward more deprived populations across all metrics. For example, the least-deprived quintile accounts for 12.2% (Ta) and 2.5% (WBGT) of total exposure duration, whereas the most-deprived quintile accounts for 21.5% (Ta) and 28.6% (WBGT), with an 11.4-fold contrast for WBGT. The magnitude of inequality also varies by metric: LST is closest to proportionality, whereas humidity-sensitive indices (HI and WBGT) show the largest disparities; under absolute thresholds, the most-deprived quintile's HI exposure duration is 40.1 times that of the least-deprived quintile (figure S13(b)). Under relative thresholds, the pattern reverses: the least-deprived quintile contributes ∼25% of exposure duration (e.g. 25.8% for Ta and 24.2% for WBGT), whereas the most-deprived quintile contributes only 18.6%–18.7%. Intensity (person-day-degrees) shows the same reversal, often with larger departures from proportionality (figures S13(a), (c)).

This reversal is clearest at the Mediterranean-wide scale, with more mixed subregional patterns (figure S14). In West Asia, exposure duration remains concentrated toward more deprived populations under both threshold frameworks, whereas in Europe, relative-threshold burdens are close to proportional. In North Africa, relative-threshold exposure duration tends to shift toward less-deprived groups. The Mediterranean-wide reversal therefore mainly reflects contrasts between the Global North (Europe) and South (West Asia and North Africa), rather than a uniform within-region flip.

Bivariate maps of WBGT exposure duration and deprivation illustrate the spatial co-occurrence underlying these curves (figures 5(b)–(c)). Under absolute thresholds, high exposure duration more often co-occurs with high deprivation in parts of North Africa and the Middle East (notably Syria, Tunisia, and Morocco), with 8.9% of evaluated pixels jointly classified as high exposure duration and high deprivation (figure 5(b)). Under relative thresholds, high exposure duration expands

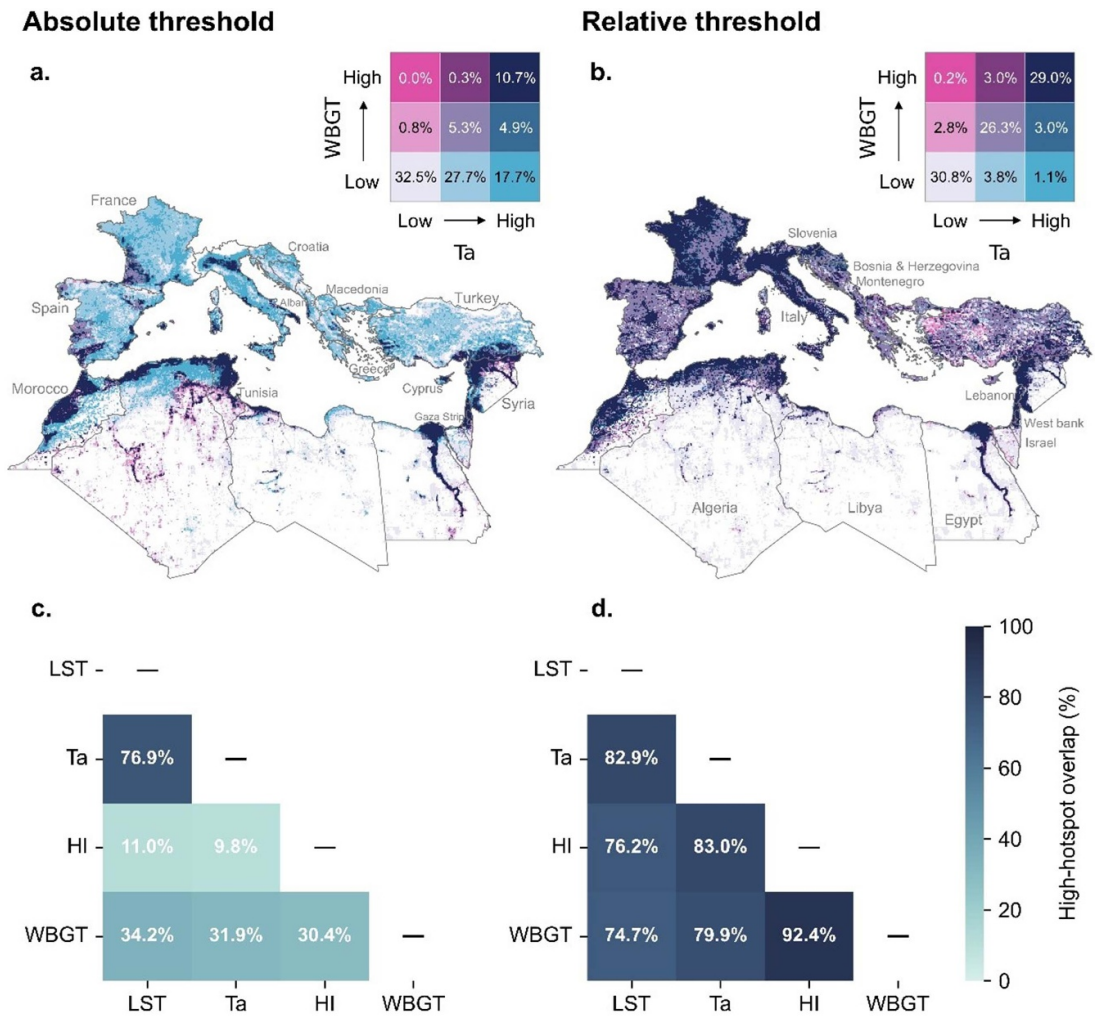

Figure 4. Spatial agreement of exposure duration between metrics under absolute and relative thresholds. (a) and (b) bivariate tercile classification of Ta and WBGT exposure duration under (a) absolute and (b) relative thresholds. For each metric, terciles (low/medium/high) are computed using pixels with positive exposure duration within the evaluated pixel set, defined as pixels where both metrics are available and at least one metric has duration >0; combining terciles yields nine joint classes. Maps are displayed at 10 km for visual clarity; all statistics are computed at the 1 km resolution. (c) and (d) Pairwise high-hotspot overlap (%) across heat metrics (LST, Ta, HI, WBGT) under (c) absolute thresholds and (d) relative thresholds, defined as the number of pixels classified as high (top-tercile) by both metrics divided by the number classified as high by at least one metric (the high-union). Values approach 100% when high-hotspot footprints fully overlap.

across populous western and southern Europe, where deprivation is generally low to moderate, increasing the high-exposure-duration/low-deprivation class from 16.9% to 20.5% (figure 5(c)). The same qualitative shift appears for LST, Ta, and HI (figure S15).

City-level rankings further translate this redistribution pattern into decision-relevant units (figure 6). For WBGT, switching from absolute to relative thresholds almost completely reorders city rankings (Spearman $\rho = 0.01$; figure 6(a)), with the highest-burden cities shifting from more deprived North African settings toward less-deprived but highly populated European cities, especially in Italy and France (figure 6(d)). Rank agreement between Ta and WBGT is higher under the relative threshold ($\rho = 0.74$; figure 6(b)) than under the absolute threshold ($\rho = 0.59$; figure 6(c)), consistent with the stronger hotspot concordance observed at the pixel scale. Together, these results show that metric–threshold choices can reshape exposure–deprivation patterns and reorder which cities emerge as high-burden targets, with direct implications for heat-action planning [69].

4. Discussion

This study shows that Mediterranean heat exposure estimates are sensitive to metric and threshold choice. In summer 2022, these choices reshaped regional exposure patterns, inequality signals, and city rankings. They therefore act as hotspot identification rules, not merely technical settings.

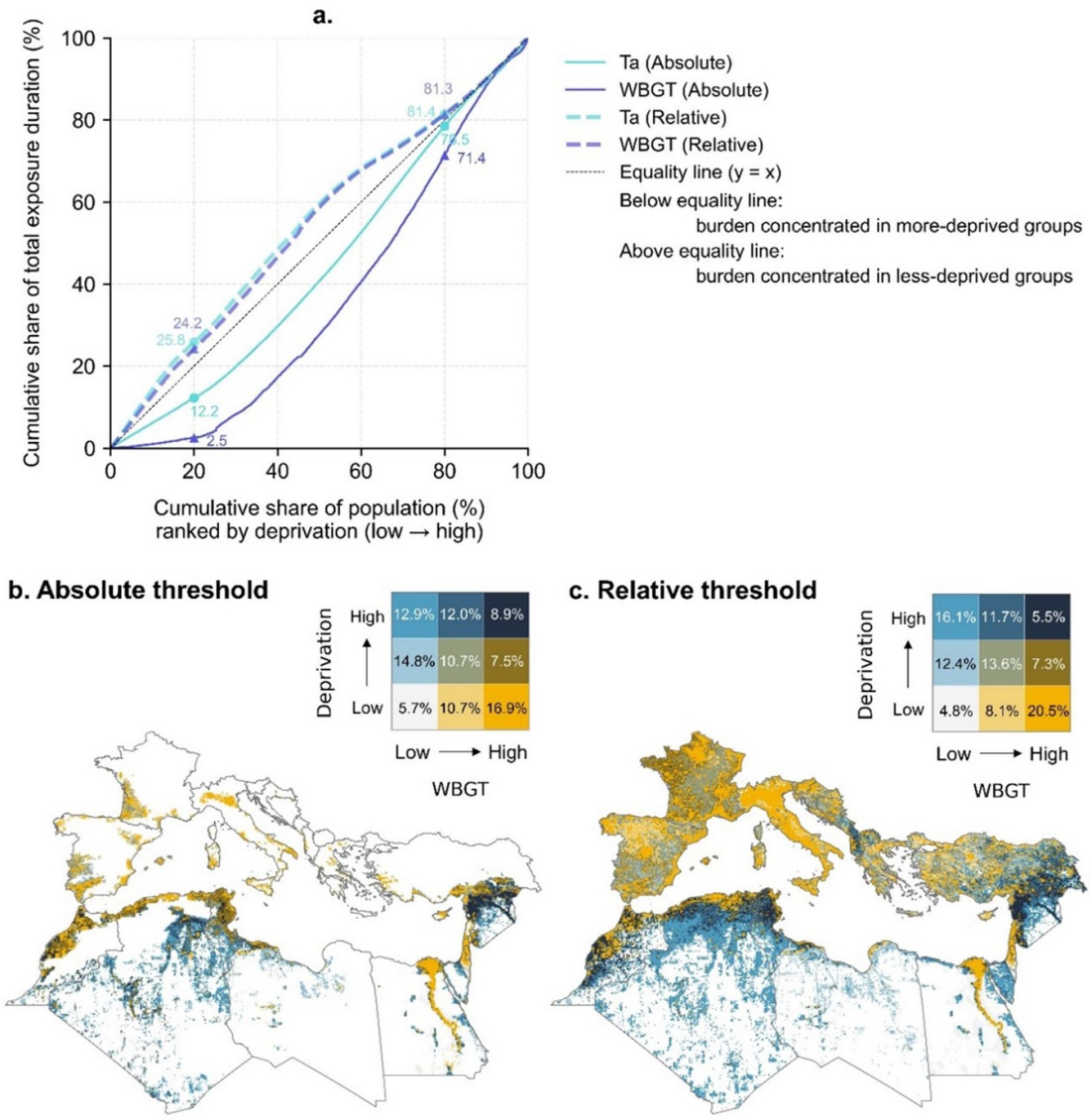

Figure 5. Socioeconomic inequality and spatial co-occurrence of heat exposure and deprivation. (a) Deprivation-ranked cumulative share curves for total exposure duration (person-days). Populations are ordered from low to high deprivation. The 45° line denotes proportional burden; curves below (above) indicate exposure duration concentrated toward more- (less-) deprived groups. (b) and (c) bivariate maps of WBGT exposure duration and deprivation under (b) absolute and (c) relative thresholds. WBGT exposure duration and deprivation are each grouped into three equal-frequency terciles (low/medium/high) using pixels with positive WBGT exposure duration and GRDI; paired terciles yield nine joint classes. Numbers in the 3 × 3 matrices denote the fraction (%) of classified pixels in each class.

4.1. Metric sensitivity under absolute versus relative extremes

A central challenge in heat exposure research is that no single metric simultaneously maximizes physiological relevance, spatial granularity, and scalability. HI and WBGT incorporate humidity, and WBGT also includes radiation and wind, but their urban-scale application is often constrained by station sparsity, instrument cost, or coarse gridded products that do not resolve urban signals (e.g. ERA5). By contrast, satellite-derived LST provides spatially detailed information on intra-urban thermal heterogeneity, but it measures surface rather than near-surface air temperature and therefore has a limited relationship to human heat load [15, 70]. Previous work in the United States similarly found that LST captured the qualitative spatial patterns of Ta and HI but overstated the magnitude of disparities [40].

In our analysis, this trade-off is most evident under absolute thresholds. Temperature-only metrics (Ta, LST) produce broad exceedance footprints, whereas composite indices (HI and WBGT) concentrate exposure in humid coastal zones and deltas [29, 71]. Under relative thresholds, these inter-metric contrasts largely diminish. By standardizing extremeness against local climatology, percentile-based thresholds reduce the influence of metric-specific physical sensitivities on hotspot

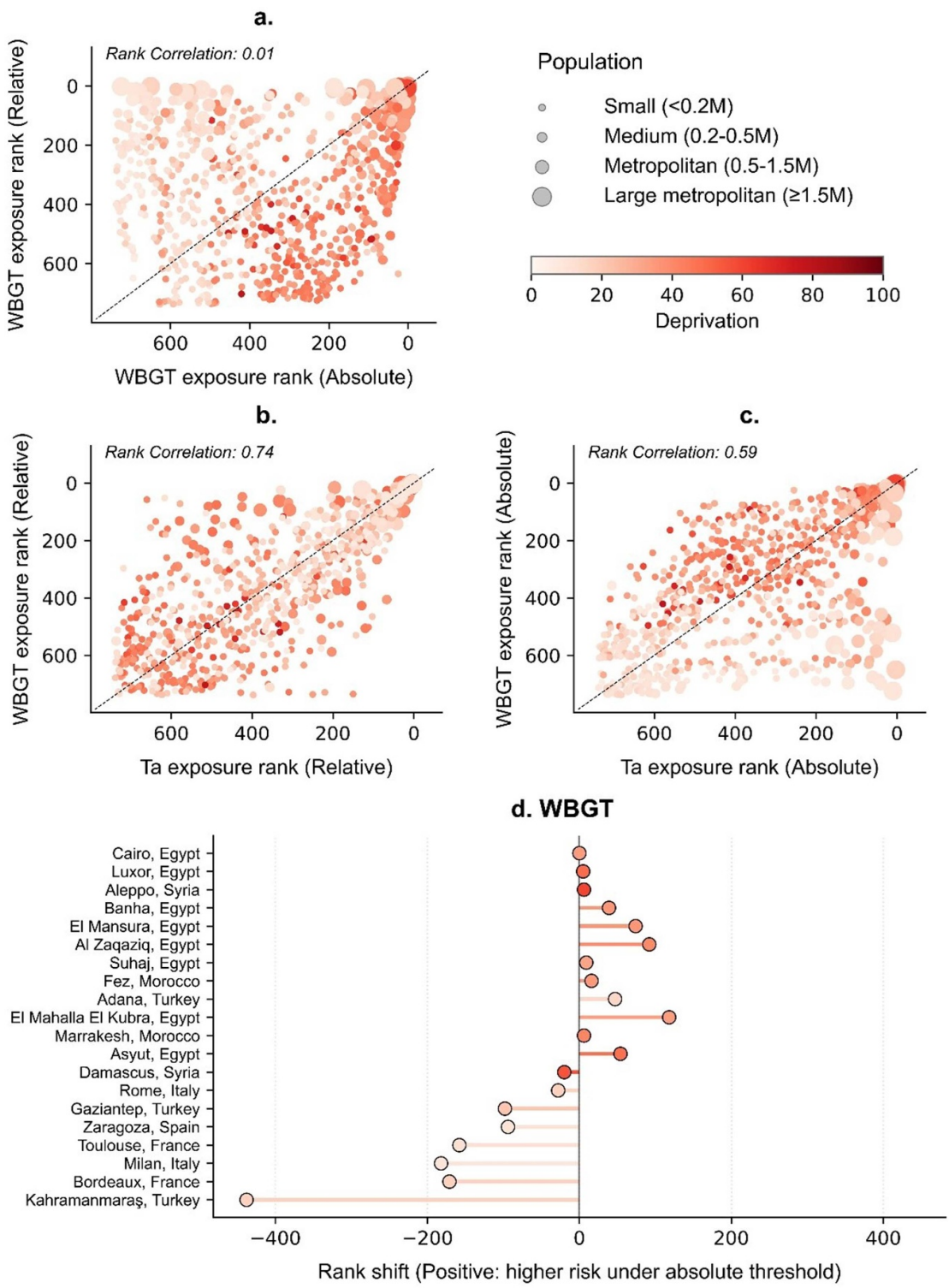

Figure 6. City ranking shifts across heat metrics and thresholds. (a) Rank–rank comparison of city WBGT exposure duration under absolute versus relative thresholds (rank 1 = highest burden). (b) and (c) rank–rank comparisons of city exposure duration ranked by Ta versus WBGT under the (b) relative and (c) absolute thresholds. The dashed line denotes equal ranks. Points are colored by mean deprivation (GRDI, 0–100) and sized by city population class. Spearman's rank correlations indicate near-complete reordering of WBGT-based city rankings across threshold frameworks (a; $\rho = 0.01$), but stronger cross-metric agreement under the relative threshold (b; $\rho = 0.74$) than under the absolute threshold (c; $\rho = 0.59$). (d) WBGT rank shifts for the union of top-10 cities under the absolute and relative thresholds. Rank shift = rank(relative)—rank(absolute); positive values indicate higher burden under the absolute thresholds, whereas negative values indicate higher burden under the relative thresholds. Colors are as in panels (a)–(c).

identification and yield more similar regional patterns across metrics.

This convergence, however, does not imply that composite indices are interchangeable. HI was developed for U.S. public guidance and reflects context-specific assumptions about how humidity modifies perceived heat [20, 44, 56]. WBGT, although more comprehensive in terms of factors considered and widely used, is also interpreted through application-specific thresholds, particularly in occupational settings [61, 62]. The weaker cross-metric agreement involving HI in our results should therefore not be interpreted simply as model failure. Rather, it suggests that combined heat-stress indices developed for one context may not transfer cleanly across climates, populations, and policy applications [20]. Determining which metric best represents thermal strain for Mediterranean populations would require validation against physiological measurements or health outcomes, which is beyond the scope of this exposure-focused study.

Within these constraints, the stronger cross-metric similarity under relative thresholds suggests that LST can serve as a widely available, spatially granular proxy for anomaly-based hotspot identification at the regional scale. This does not imply that LST can substitute for within-city air-temperature exposure. Because our Ta, HI, and WBGT estimates are derived from ERA5-Land, they do not resolve intra-urban variability, preventing a robust evaluation of LST for within-city exposure estimation. Such an assessment would require independent city-scale air-temperature data, such as dense station networks or urban-resolving products, to derive context-specific LST–Ta relationships.

4.2. Threshold-driven shifts in hotspot geography and decision relevance

Hotspot identification is highly sensitive to the threshold framework. Under absolute thresholds, Ta identifies broad exceedance footprints extending into arid interiors, whereas WBGT concentrates high exposure along humid coastlines and the Nile Delta, where moisture, radiation, and wind jointly elevate heat load. Under relative thresholds, patterns converge because each metric is evaluated against its local baseline, thereby shifting hotspots toward populous parts of southern Europe that experienced strong departures from baseline in 2022 [37, 72, 73]. This contrast also appears in 2021, 2023, 2024, and 2025 (figure S16): despite interannual variation in exposure extent, absolute thresholds preserve larger spatial differences between Ta and WBGT, whereas relative thresholds yield more similar hotspot patterns.

This anomaly-based interpretation is consistent with epidemiological evidence from 2022: the largest summer-mean temperature anomalies (relative to the 1991–2020 climatological baseline) clustered in southwestern Europe, whereas heat-related mortality was highest in several Mediterranean countries, notably Italy, Greece, and Spain [37, 73]. Given cross-country differences in vulnerability and adaptation, such divergence is expected and suggests that anomaly-based hotspots do not necessarily coincide with where heat-health burdens are greatest. Our national Ta totals illustrate this divergence: total exposure duration is 4.3× higher under the absolute than the relative framework, and some countries remain high-burden under absolute thresholds even when they rank lower under anomaly-based definitions (Italy and Spain ≈2.2×; Greece ≈6.5×). Together with the 2022 mortality evidence [37], these findings underscore that the most anomalous places are not necessarily the most hazardous.

Importantly, anomaly-based exceedances can occur at moderate absolute levels, while fixed thresholds can understate unusual heat in historically cooler places that may be less heat-prepared because of more limited access to cooling, lower air-conditioning prevalence, or weaker behavioral and institutional adaptation. We therefore interpret absolute and relative thresholds as complementary lenses for distinct heat-action objectives—fixed-threshold protection versus anomaly-based early warning.

This distinction is also evident in city-level targeting: the near-complete reordering of WBGT-based city rankings across threshold frameworks (Spearman $\rho = 0.01$) shows that candidate intervention targets can shift substantially depending on how extremes are defined. For heat warning and intervention design, candidate hazard metrics and thresholds should therefore be evaluated against local health outcomes at the relevant decision scale, since predictive performance can be region- and scale-dependent [74].

4.3. Threshold-dependent exposure gradients across deprivation

A key result is that the Mediterranean-wide exposure–deprivation gradient reverses across threshold frameworks. Under absolute thresholds, exposure duration and intensity are concentrated in more deprived populations of North Africa and the Middle East, especially for humidity-sensitive indices, consistent with broader environmental-justice evidence that heat hazards and limited protective resources often co-occur in disadvantaged settings [7, 75, 76]. By contrast, under relative thresholds, anomaly-defined exceedances expand across densely populated European urban areas, shifting a larger share of exposure toward less-deprived quintiles. A multi-year sensitivity check using Ta and WBGT supports the same interpretation (figure S17): across 2021, 2023, 2024, and 2025, absolute-threshold curves remain more concentrated toward deprived populations, whereas relative-threshold curves shift

closer to the equality line, although the strength of this shift varies by year.

This Mediterranean-wide reversal, however, is not uniform across subregions. Continent-stratified curves (figure S14) show that West Asia remains skewed toward more deprived populations under both frameworks, Europe is close to proportionality under relative thresholds, and North Africa tends to shift toward less-deprived groups. Therefore, the Mediterranean-wide reversal mainly reflects contrasts between subregions rather than a consistent within-subregion flip. Although absolute and relative thresholds yield different inequality patterns in all subregions, the direction and magnitude of these differences vary by region. These results suggest that heat-exposure inferences are consistently sensitive to threshold definition across diverse climatic and socioeconomic settings, and that regional inequality patterns should be interpreted alongside subregional analyses.

This distinction matters for environmental-justice interpretation. Relative thresholds are useful for identifying unusual heat that may stress local public health and infrastructure systems, but they do not encode vulnerability or adaptive capacity. Because adaptive capacity can differ systematically by socioeconomic status, including through unequal access to cooling and other heat-protective resources [77], anomaly-based exposure should not be interpreted as a direct proxy for inequality-relevant health risk [78]. Moreover, standardizing by local climatology can down-weight persistently high baseline heat in chronically hot regions, potentially obscuring entrenched structural burdens. These results do not imply that one framework is inherently better; rather, methodological choice determines which dimensions of heat burden become most visible. Accordingly, exposure patterns should be interpreted jointly with socioeconomic, vulnerability, and adaptation indicators to avoid masking persistent burdens in more deprived populations.

4.4. Limitations and future directions

Although this is the first Mediterranean-wide comparison of population exposure across heat metrics and threshold frameworks, several limitations remain. We quantify environmental exposure rather than health outcomes; translating exposure into health impacts requires vulnerability, adaptation, and epidemiological evidence [79]. ERA5-based inputs do not explicitly resolve urban canopy processes [80, 81], and our estimates also do not capture daily mobility. However, a comparison with an urban-adjusted 1 km air temperature product [82] shows strong correspondence for local-time daily maximum air temperature (figure S18; $R^2 = 0.79$), suggesting that regional spatial patterns remain robust even if within-city variability is conservative. Future work should extend this comparison to other regions, test metric–threshold combinations against local health outcomes, and examine whether conclusions based on regional summaries hold at subregional and city scales. This would clarify which exposure definitions are most useful for warning, targeting, and heat-equity assessment.

5. Conclusions

Metric and threshold choices act as hotspot identification rules, reshaping exposure totals, hotspot alignment, inequality gradients, and city rankings across the Mediterranean. Absolute thresholds yield large differences across metrics and weak hotspot overlap, whereas relative thresholds yield more similar totals and stronger agreement. Inequality signals can also reverse: absolute thresholds concentrate exposure in more deprived settings, while relative thresholds shift exposure toward less-deprived but populous southern Europe, and city rankings based on WBGT exposure duration are almost completely reordered. We therefore recommend routine dual reporting of absolute and relative exposures to support more robust heat-action planning and to reduce overreliance on any single exposure definition.

Acknowledgment

This work was supported by the National Aeronautics and Space Administration (NASA) (Grant Numbers 80NSSC24K1247 and 80NSSC24K1039). T.C.'s contribution was supported by a NASA Interdisciplinary Research in Earth Science grant (Grant Number 80NSSC24K0505). L.C. acknowledges UW Data Science Postdoctoral Fellows Program at the eScience Institute, University of Washington, for contributing to professional development and interdisciplinary research community.

Data availability statement

The data that support the findings of this study are openly available at the following URL/DOI: https://doi.org/10.5281/zenodo.19656973 [83].

Supplementary information available at https://doi.org/10.1088/1748-9326/ae6711/data1.

CRediT authorship contribution statement

Liutao Chen: Conceptualization, Methodology, Software, Writing—original draft, Writing—review & editing, Visualization, Formal analysis, Investigation. Tirthankar 'TC' Chakraborty: Methodology, Writing—review & editing, Formal analysis, Supervision. Joan A. Casey: Writing—review & editing, Investigation. Ching-Hsuan Huang: Writing—review & editing, Investigation. Tzu-Hsin Karen Chen: Conceptualization, Methodology, Writing—review & editing, Formal analysis, Supervision, Project administration, Funding acquisition.

Conflict of interest

The authors declare no conflict of interest.

ORCID iDs

Liutao Chen 0000-0002-4206-6441
TC Chakraborty 0000-0003-1338-3525
Joan A Casey 0000-0002-9809-4695
Ching-Hsuan Huang 0000-0002-7283-7032
Tzu-Hsin Karen Chen 0000-0002-0343-6147

References

[1] Seneviratne S I, Zhang X, Adnan M, Badi W, Dereczynski C, Luca A D, Ghosh S, Iskandar I, Kossin J and Lewis S 2021 Weather and climate extreme events in a changing climate *Climate Change 2021: The Physical Science Basis. Contribution of Working Group I to the Sixth Assessment Report of the Intergovernmental Panel on Climate Change* (Cambridge United Kingdom) pp 1513–766

[2] Ebi K L, Capon A, Berry P, Broderick C, de Dear R, Havenith G, Honda Y, Kovats R S, Ma W and Malik A 2021 Hot weather and heat extremes: health risks *Lancet* **398** 698–708

[3] Lüthi S, Fairless C, Fischer E M, Scovronick N, Armstrong B, Coelho M D S Z S, Guo Y L, Guo Y, Honda Y and Huber V 2023 Rapid increase in the risk of heat-related mortality *Nat. Commun.* **14** 4894

[4] Tuholske C, Caylor K, Funk C, Verdin A, Sweeney S, Grace K, Peterson P and Evans T 2021 Global urban population exposure to extreme heat *Proc. Natl Acad. Sci. USA* **118** e2024792118

[5] Bobde V, Ayegbusi K, Akinsanola A A, Adeyeri O E, Morakinyo T E and Adebiyi A A 2025 Anthropogenic warming is accelerating recent heatwaves in Africa *Commun. Earth Environ.* **6** 578

[6] Zhang J, You Q, Ren G, Ullah S, Normatov I and Chen D 2023 Inequality of global thermal comfort conditions changes in a warmer world *Earth's Future* **11** e2022EF003109

[7] Hsu A, Sheriff G, Chakraborty T and Manya D 2021 Disproportionate exposure to urban heat island intensity across major US cities *Nat. Commun.* **12** 2721

[8] De Perez E C, Van Aalst M, Bischiniotis K, Mason S, Nissan H, Pappenberger F, Stephens E, Zsoter E and Van Den Hurk B 2018 Global predictability of temperature extremes *Environ. Res. Lett.* **13** 054017

[9] O'Neill B C, Carter T R, Ebi K, Harrison P A, Kemp-Benedict E, Kok K, Kriegler E, Preston B L, Riahi K and Sillmann J 2020 Achievements and needs for the climate change scenario framework *Nat. Clim. Change* **10** 1074–84

[10] Broadbent A M, Krayenhoff E S and Georgescu M 2020 The motley drivers of heat and cold exposure in 21st century US cities *Proc. Natl Acad. Sci. USA* **117** 21108–17

[11] Vanos J K, Baldwin J W, Jay O and Ebi K L 2020 Simplicity lacks robustness when projecting heat-health outcomes in a changing climate *Nat. Commun.* **11** 6079

[12] Massaro E, Schifanella R, Piccardo M, Caporaso L, Taubenböck H, Cescatti A and Duveiller G 2023 Spatially-optimized urban greening for reduction of population exposure to land surface temperature extremes *Nat. Commun.* **14** 2903

[13] Iungman T, Khomenko S, Barboza E P, Cirach M, Gonçalves K, Petrone P, Erbertseder T, Taubenböck H, Chakraborty T and Nieuwenhuijsen M 2024 The impact of urban configuration types on urban heat islands, air pollution, CO_2 emissions, and mortality in Europe: a data science approach *Lancet Planet. Health* **8** e489–e505

[14] Li G, Cao Y, Fang C, Sun S, Qi W, Wang Z, He S and Yang Z 2025 Global urban greening and its implication for urban heat mitigation *Proc. Natl Acad. Sci. USA* **122** e2417179122

[15] Zhan W, Bechtel B, Du H, Chakraborty T, Kotthaus S, Krayenhoff E S, Martilli A, Naserikia M, Nazarian N and Roth M 2025 Satellite-derived land surface temperatures strongly mischaracterise urban heat hazard (arXiv:2509.16568)

[16] Sherwood S C and Huber M 2010 An adaptability limit to climate change due to heat stress *Proc. Natl Acad. Sci.* **107** 9552–5

[17] Popp Z, Wing I S, Lane K J and Wellenius G A 2025 A US heat disaster? Intersection of social vulnerability and temperature extremes exacerbated by mid-century climate change and population shifts *Environ. Res.: Health* **3** 025009

[18] Raymond C, Matthews T and Horton R M 2020 The emergence of heat and humidity too severe for human tolerance *Sci. Adv.* **6** eaaw1838

[19] Jacobs C, Singh T, Gorti G, Iftikhar U, Saeed S, Syed A, Abbas F, Ahmad B, Bhadwal S and Siderius C 2019 Patterns of outdoor exposure to heat in three South Asian cities *Sci. Total Environ.* **674** 264–78

[20] Simpson C H, Brousse O, Ebi K L and Heaviside C 2023 Commonly used indices disagree about the effect of moisture on heat stress *npj Clim. Atmos. Sci.* **6** 78

[21] Occupational Safety and Health Administration 2026 Heat hazard recognition (available at: www.osha.gov/heat-exposure/hazards).

[22] Wang Y, Chen L, Song Z, Huang Z, Ge E, Lin L and Luo M 2019 Human-perceived temperature changes over South China: long-term trends and urbanization effects *Atmos. Res.* **215** 116–27

[23] ISO 2017 *Ergonomics of the thermal environment—assessment of heat stress using the WBGT (wet bulb globe temperature) index* (International Organization for Standardization)

[24] Coco A, Jacklitsch B, Williams J, Kim J-H, Musolin K and Turner N 2016 Criteria for a recommended standard: occupational exposure to heat and hot environments (DHHS (NIOSH) Publication)

[25] Sheridan S C and Allen M J 2018 Temporal trends in human vulnerability to excessive heat *Environ. Res. Lett.* **13** 043001

[26] Curriero F C, Heiner K S, Samet J M, Zeger S L, Strug L and Patz J A 2002 Temperature and mortality in 11 cities of the eastern United States *Am. J. Epidemiol.* **155** 80–87

[27] Chandra N S V and Lee J K W 2025 A systematic review of heat health warning systems: enhancing the framework

towards effective health outcomes *Curr. Environ. Health Rep.* **12** 31
[28] Li L and Zha Y 2020 Population exposure to extreme heat in China: frequency, intensity, duration and temporal trends *Sustain. Cities Soc.* **60** 102282
[29] Freychet N, Hegerl G C, Lord N S, Lo Y E, Mitchell D and Collins M 2022 Robust increase in population exposure to heat stress with increasing global warming *Environ. Res. Lett.* **17** 064049
[30] Oleson K W, Monaghan A, Wilhelmi O, Barlage M, Brunsell N, Feddema J, Hu L and Steinhoff D 2015 Interactions between urbanization, heat stress, and climate change *Clim. Change* **129** 525–41
[31] McAllister C, Stephens A and Milrad S M 2022 The heat is on: observations and trends of heat stress metrics during Florida summers *J. Appl. Meteorol. Climatol.* **61** 277–96
[32] Tuel A and Eltahir E A 2020 Why is the Mediterranean a climate change hot spot? *J. Clim.* **33** 5829–43
[33] Ali E, Cramer W, Carnicer J, Georgopoulou E, Hilmi N J M, Cozannet G L and Lionello P 2022 Cross-Chapter Paper 4: mediterranean Region *Climate Change 2022: Impacts, Adaptation and Vulnerability. Contribution of Working Group II to the Sixth Assessment Report of the Intergovernmental Panel on Climate Change* (Cambridge University Press) pp 2233–72
[34] W.M. Organization 2025 State of climate in the Arab region 2024
[35] Desa U 2019 United nations department of economic and social affairs(Population Division World Population Prospects)
[36] Theys J, Lacroix D and Amine K 2025 MED 2050, the Mediterranean by 2050, A foresight by plan bleu—summary (Plan Bleu)
[37] Ballester J, Quijal-Zamorano M, Méndez Turrubiates R F, Pegenaute F, Herrmann F R, Robine J M, Basagaña X, Tonne C, Antó J M and Achebak H 2023 Heat-related mortality in Europe during the summer of 2022 *Nat. Med.* **29** 1857–66
[38] Xu Z, FitzGerald G, Guo Y, Jalaludin B and Tong S 2016 Impact of heatwave on mortality under different heatwave definitions: a systematic review and meta-analysis *Environ. Int.* **89** 193–203
[39] Barriopedro D, García-Herrera R, Ordónez C, Miralles D G and Salcedo-Sanz S 2023 Heat waves: physical understanding and scientific challenges *Rev. Geophys.* **61** e2022RG000780
[40] Chakraborty T, Newman A J, Qian Y, Hsu A and Sheriff G 2023 Residential segregation and outdoor urban moist heat stress disparities in the united states *One Earth* **6** 738–50
[41] Center for International Earth Science Information Network (CIESIN), Columbia University 2022 Global gridded relative deprivation index (GRDI), version 1 (NASA Socioeconomic Data and Applications Center (SEDAC)) (https://doi.org/10.7927/3xxe-ap97)
[42] Pesaresi M, Schiavina M, Politis P, Freire S, Krasnodębska K, Uhl J H, Carioli A, Corbane C, Dijkstra L and Florio P 2024 Advances on the global human settlement layer by joint assessment of Earth observation and population survey data *Int. J. Digit. Earth* **17** 2390454
[43] Li Y, Svenning J-C, Zhou W, Zhu K, Abrams J F, Lenton T M, Ripple W J, Yu Z, Teng S N and Dunn R R 2024 Green spaces provide substantial but unequal urban cooling globally *Nat. Commun.* **15** 7108
[44] NOAA 1990 The heat index equation (available at: www.wpc.ncep.noaa.gov/html/heatindex_equation.shtml)
[45] Liljegren J C, Carhart R A, Lawday P, Tschopp S and Sharp R 2008 Modeling the wet bulb globe temperature using standard meteorological measurements *J. Occup. Environ. Hyg.* **5** 645–55
[46] Carter A W, Zaitchik B F, Gohlke J M, Wang S and Richardson M B 2020 Methods for estimating wet bulb globe temperature from remote and low-cost data: a comparative study in central Alabama *GeoHealth* **4** e2019GH000231
[47] Bernard T E 1999 Prediction of workplace wet bulb global temperature *Appl. Occup. Environ. Hyg.* **14** 126–34
[48] Brunner L and Voigt A 2024 Pitfalls in diagnosing temperature extremes *Nat. Commun.* **15** 2087
[49] Zhang Q, Gu L, Jia B and Fang Y 2024 Summertime compound heat extremes change and population heat exposure distribution in China *J. Cleaner Prod.* **485** 144381
[50] Manoli G, Fatichi S, Schläpfer M, Yu K, Crowther T W, Meili N, Burlando P, Katul G G and Bou-Zeid E 2019 Magnitude of urban heat islands largely explained by climate and population *Nature* **573** 55–60
[51] Dowell M, Bernard S, Kilsedar C, Gianinetto M, Speyer O, Kuffer M, Grecchi R, Gliottone I and Melchiorri M 2025 Earth observation in support of Eu policies for urban climate adaptation
[52] World Bank 2024 *Urban Overheating and Adaptation Measures—An Analysis at EU, National, and Local Level (English)* ed W B Group (World Bank)
[53] Martilli A, Roth M and Chow W T 2020 Summer average urban-rural surface temperature differences do not indicate the need for urban heat reduction
[54] Vicedo-Cabrera A M, Scovronick N, Sera F, Royé D, Schneider R, Tobias A, Astrom C, Guo Y, Honda Y and Hondula D 2021 The burden of heat-related mortality attributable to recent human-induced climate change *Nat. Clim. Change* **11** 492–500
[55] Gasparrini A, Guo Y, Hashizume M, Lavigne E, Zanobetti A, Schwartz J, Tobias A, Tong S, Rocklöv J and Forsberg B 2015 Mortality risk attributable to high and low ambient temperature: a multicountry observational study *Lancet* **386** 369–75
[56] Baldwin J W, Benmarhnia T, Ebi K L, Jay O, Lutsko N J and Vanos J K 2023 Humidity's role in heat-related health outcomes: a heated debate *Environ. Health Perspect.* **131** 055001
[57] Matthies F 2008 Heat-health action plans: guidance (World Health Organization)
[58] Choi H M and Bell M L 2023 Heat-mortality relationship in North Carolina: comparison using different exposure methods *J. Expo. Sci. Environ. Epidemiol.* **33** 637–45
[59] Luber G and McGeehin M 2008 Climate change and extreme heat events *Am. J. Prev. Med.* **35** 429–35
[60] Fischer E M and Schär C 2010 Consistent geographical patterns of changes in high-impact European heatwaves *Nat. Geosci.* **3** 398–403
[61] Budd G M 2008 Wet-bulb globe temperature (WBGT)—its history and its limitations *J. Sci. Med. Sport* **11** 20–32
[62] Ioannou L G, Tsoutsoubi L, Mantzios K, Vliora M, Nintou E, Piil J F, Notley S R, Dinas P C, Gourzoulidis G A and Havenith G 2022 Indicators to assess physiological heat strain–part 3: multi-country field evaluation and consensus recommendations *Temperature* **9** 274–91
[63] NWS Wet bulb globe temperature forecasts transition to operational (available at: www.weather.gov/news/220106-wet-bulb-globe)
[64] Center for International Earth Science Information Network (CIESIN), Columbia University 2022 Documentation for the global gridded relative deprivation index (GRDI), version 1 (NASA Socioeconomic Data and Applications Center (SEDAC)) (https://doi.org/10.7927/xwf1-k532)
[65] Venter Z S, Chakraborty T and Lee X 2021 Crowdsourced air temperatures contrast satellite measures of the urban heat island and its mechanisms *Sci. Adv.* **7** eabb9569
[66] Gorelick N, Hancher M, Dixon M, Ilyushchenko S, Thau D and Moore R 2017 Google Earth engine: planetary-scale geospatial analysis for everyone *Remote Sens. Environ.* **202** 18–27
[67] Chen J, Qian Y, Chakraborty T C and Yang Z 2024 Complexities of urban impacts on long-term seasonal trends in a mid-sized arid city *Environ. Res. Commun.* **6** 021004
[68] Nogueira M, Hurduc A, Ermida S, Lima D C, Soares P M, Johannsen F and Dutra E 2022 Assessment of the Paris

urban heat island in ERA5 and offline SURFEX-TEB (v8. 1) simulations using METEOSAT land surface temperature product, geoscientific model development discussions 2022 pp 1–29
[69] Royé D, Janoš T, Paniello-Castillo B, Chen Z-Y, Thompson A T, Ruiz-Cabrejos J, Quijal-Zamorano M, Tobias A, Shartova N and Antó J M 2026 Rethinking early warning systems for the health effects of extreme heat *Nat. Health* **1** 6–8
[70] Briegel F, Pinto J G and Christen A 2025 Is satellite land surface temperature an appropriate proxy for intra-urban variability of daytime heat stress? *Remote Sens. Environ.* **331** 115045
[71] Kong Q, Jing R, Raymond C, Tuholske C, Heft-Neal S, Wagner Z, Wang Z, Zimmer A, Huber M and Bendavid E 2025 Spatial patterns of historical changes in human heat stress disagree across metrics *Geophys. Res. Lett.* **52** e2025GL117966
[72] Gallo E, Quijal-Zamorano M, Méndez Turrubiates R F, Tonne C, Basagaña X, Achebak H and Ballester J 2024 Heat-related mortality in Europe during 2023 and the role of adaptation in protecting health *Nat. Med.* **30** 3101–5
[73] Janoš T, Quijal-Zamorano M, Shartova N, Gallo E, Méndez Turrubiates R F, Denisse Beltrán Barrón N, Peyrusse F and Ballester J 2025 Heat-related mortality in Europe during 2024 and health emergency forecasting to reduce preventable deaths *Nat. Med.* **31** 1–10
[74] Wilson A J, Bressler R D, Ivanovich C, Tuholske C, Raymond C, Horton R M, Sobel A, Kinney P, Cavazos T and Shrader J G 2024 Heat disproportionately kills young people: evidence from wet-bulb temperature in Mexico *Sci. Adv.* **10** eadq3367
[75] Slesinski S C, Matthies-Wiesler F, Breitner S, Gussmann G and Schneider A 2025 Social inequalities in exposure to heat stress and related adaptive capacity: a systematic review *Environ. Res. Lett.* **20** 033005
[76] Coelho J C, Schwartz J D, Koutrakis P and Requia W J 2025 Global socioeconomic disparities in exposure to extreme heat *Clim. Change* **178** 223
[77] van Daalen K R, Romanello M, Rocklöv J, Semenza J C, Tonne C, Markandya A, Dasandi N, Jankin S, Achebak H and Ballester J 2022 The 2022 Europe report of the lancet countdown on health and climate change: towards a climate resilient future *Lancet Public Health* **7** e942–e65
[78] López-Bueno J A, Navas-Martín M, Díaz J, Mirón I, Luna M, Sánchez-Martínez G, Culqui D and Linares C 2022 Analysis of vulnerability to heat in rural and urban areas in Spain: what factors explain heat's geographic behavior? *Environ. Res.* **207** 112213
[79] Lin Y-K, Chang C-K, Li M-H, Wu Y-C and Wang Y-C 2012 High-temperature indices associated with mortality and outpatient visits: characterizing the association with elevated temperature *Sci. Total Environ.* **427** 41–49
[80] Chen L, Yang J and Zheng X 2024 Modelling the impact of building energy consumption on urban thermal environment: the bias of the inventory approach *Urban Clim.* **53** 101802
[81] Pigliautile I, Pisello A and Bou-Zeid E 2020 Humans in the city: representing outdoor thermal comfort in urban canopy models *Renew. Sustain. Energy Rev.* **133** 110103
[82] Zhang T, Zhou Y, Zhao K, Zhu Z, Chen G, Hu J and Wang L 2022 A global dataset of daily maximum and minimum near-surface air temperature at 1 km resolution over land (2003–2020) *Earth Syst. Sci. Data* **14** 5637–49
[83] Chen L 2026 Data and Code for: Heat metrics and thresholds reshape population exposure and inequality signals *Zenodo* (https://doi.org/10.5281/zenodo.19656973)